ANNUAL REVIEWS

*Annual Review of Physical Chemistry*

# Magneto-Optical Properties of Noble Metal Nanostructures

Juniper Foxley and Kenneth L. Knappenberger Jr.

Department of Chemistry, The Pennsylvania State University, University Park, Pennsylvania, USA; email: klk260@psu.edu

Annu. Rev. Phys. Chem. 2023. 74:53–72

First published as a Review in Advance on January 25, 2023

The *Annual Review of Physical Chemistry* is online at physchem.annualreviews.org

https://doi.org/10.1146/annurev-physchem-062322-043108





## Keywords

noble metal nanostructures, plasmon-mediated magneto-optics, superatoms, spin-polarized emission, magnetic circular photoluminescence, magnetic circular dichroism

## Abstract

The magneto-optical signatures of colloidal noble metal nanostructures, spanning both discrete nanoclusters (<2 nm) and plasmonic nanoparticles (>2 nm), exhibit rich structure-property correlations, impacting applications including photonic integrated circuits, light modulation, applied spectroscopy, and more. For nanoclusters, electron doping and single-atom substitution modify both the intensity of the magneto-optical response and the degree of transient spin polarization. Nanoparticle size and morphology also modulate the magnitude and polarity of plasmon-mediated magneto-optical signals. This intimate interplay between nanostructure and magneto-optical properties becomes especially apparent in magnetic circular dichroism (MCD) and magnetic circular photoluminescence (MCPL) spectroscopic data. Whereas MCD spectroscopy informs on a metal nanostructure's steady-state extinction properties, its MCPL counterpart is sensitive to electronic spin and orbital angular momenta of transiently excited states. This review describes the size- and structure-dependent magneto-optical properties of nanoscale metals, emphasizing the increasingly important role of MCPL in understanding transient spin properties and dynamics.

## 1. INTRODUCTION

Observations of rich magneto-optical phenomena are widespread at the nanoscale. However, perhaps no material class rivals the diversity of magneto-optical phenomena exhibited by noble metal nanostructures. Their breadth of properties results from the size-dependent evolution (**Figure 1**) from discrete electronic transitions of nanoclusters (<≈2 nm) to the collective plasmon excitations of nanoparticles (>≈2 nm). For nanoclusters, magneto-optical properties arise from the combined electronic spin and orbital angular momenta in molecular-like and superatomic orbitals (1–6). These spin-orbit coupling (SOC) effects both are large and required to account for the electronic structure of both molecular and nanocluster complexes of gold (see the sidebar titled Spin-Orbit Coupling) (7, 8). However, the magnitudes of these responses are sensitive to electron density, valence electron counts, and interatomic distances that can be modified by synthetic metal–atom and ligand substitutions (9, 10). Spin-orbit interactions are also observed in plasmonic systems, but other factors such as nanoparticle structure and orientation can significantly affect the magneto-optical response at this scale (11). The fundamental differences in the origin of the nanocluster and nanoparticle magneto-optical responses can lead to an array of applications including spin-polarized quantum emission, light polarization modulation, and enhanced

### SPIN-ORBIT COUPLING

Spin-orbit coupling (SOC) refers to the phenomenon by which the spin of an electron (*S*) interacts with its orbital angular momentum (*L*). These two quanta involve a circular movement of the electron (i.e., a circular movement of electric charge), thus inducing small magnetic dipoles in each case. These dipoles interact additively, increasing the overall angular momentum (*J*) of the system according to $J = L + S$. The magnetic dipoles may also align either parallel or antiparallel to one another, causing a slight lifting of the degeneracy of spin states belonging to a specific angular momentum. SOC may occur through different mechanisms. Generally, low-mass nuclei exhibit spin-orbit interactions that occur at the single-electron level, whereas more massive species tend to support collective coupling of all valence electrons in unfilled subshells. More details can be found in Reference 28.

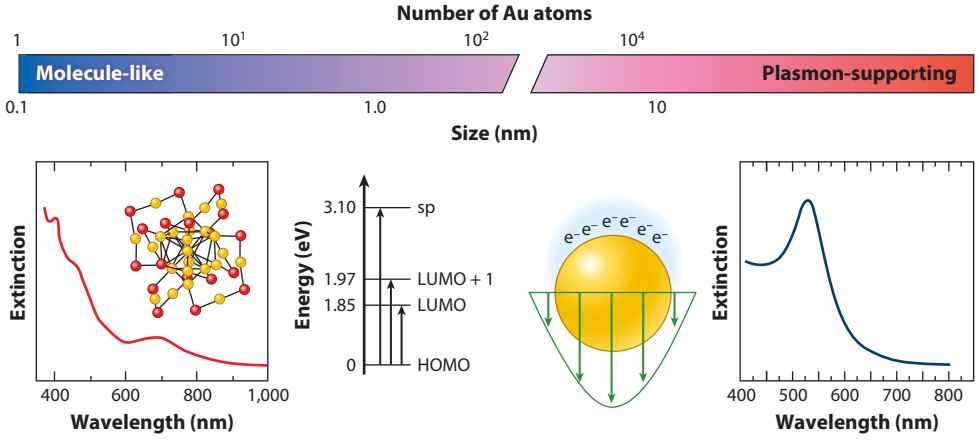


**Figure 1**

Size-dependent evolution of electronic and optical properties in metal nanostructures, from quantum-confined nanoclusters to plasmon-supporting colloidal nanoparticles. Reprinted with permission from Reference 97; copyright 2018 American Chemical Society.

magneto-optical spectroscopy, among others. As a result, facile colloidal synthesis of both nanoclusters and nanoparticles can be used to tailor magneto-optical properties with a range and level of control that would be difficult to achieve using other material platforms. Therefore, colloidal metal nanostructures are prime candidates for establishing tunable and predictive magnetic and spin-based materials.

Monolayer-protected metal clusters (MPCs) are a class of colloidal metal nanostructures that are especially well-suited for understanding the interplay between nanoscale structure and magneto-optical properties. MPCs span the nanocluster-to-nanoparticle length scales. Thiol-protected MPCs are stabilized by a combination of electronic and geometric factors and consist of three primary structural components: (*a*) an all-metal core, (*b*) protective metal–chalcogenide semirings, and (*c*) organic ligands that passivate the cluster through carbon–chalcogenide bonds (12–15). These metals exhibit both steady-state and transient magneto-optical properties that are determined by atomic-level structure (9, 16–19). Electronically excited MPC nanoclusters relax through a series of competitive internal conversion and intersystem crossing processes, resulting in varying degrees of transient spin polarization spanning visible-to-near-infrared (NIR) wavelengths (16, 20, 21). Changes to each of the three structural components have been shown to affect the transient spin polarization of MPCs (9, 16, 22, 23). These recent insights have been revealed largely through magneto-optical measurements that can characterize the spin, orbital, and SOC properties of MPC electronic states. In fact, transient and emission-based magneto-optical measurements have played a paramount role in elucidating photoluminescence (PL) mechanisms, distinguishing distinct inter- and intraband radiative recombination pathways (3, 5, 9, 18).

Early measurements to characterize the magneto-optical properties of materials relied on the use of magnetic optical rotary dispersion (MORD). MORD, much like later iterations of magneto-optical measurements, is based on the Faraday effect, wherein plane-polarized light is rotated upon transmission through a sample under an applied magnetic field (24). The creation of photoelastic modulators in the 1960s gave way to magnetic circular dichroism (MCD) as a preferred technique for measuring magneto-optical signals. MCD is a stimulated absorption technique that isolates electronic fine structure states based on preferential interactions with right circularly polarized (RCP) or left circularly polarized (LCP) light. The use of photoelastic modulators allowed for the facile generation of alternating polarization schemes, which simplified isolation of the sample magneto-optical spectrum from background and artifacts (25). Traditionally described in the context of Zeeman splitting, these methods provide valuable information about the SOC of atomic and molecular orbitals.

Major breakthroughs in understanding the interplay between magneto-optical properties and structure were precipitated by the development of magnetic circular PL (MCPL). MCPL is the spontaneous emission analog of MCD, but it is a distinguished and indispensable resource for the characterization of nanostructures because it affords the ability to isolate magneto-optical signatures of transient and excited states (1–6, 9, 10). MCPL can also be used in the time domain and to resolve electronic and nuclear dynamics that affect the spin-dependent and magneto-optical signatures of the material (26). In combination, MCD and MCPL have been used to understand the magneto-optical excitation, spin dynamics, and emission spectra of metal nanoclusters and plasmonic nanoparticles. In parallel, metal nanoparticle synthesis has advanced to achieve structural control at the atomic level (12–15). Hence, a predictive understanding of the impact of precision colloidal synthesis on the magneto-optical spectra of metal nanostructures could lead to an improved mechanistic understanding of energy flow through confined metals, as well as novel applications that rely on polarization-selective light absorption and/or emission such as photonic circuits, spin-polarized photon emission, and enhanced chiroptical and magneto-optical spectroscopy.

Here, we provide a comprehensive review of the magneto-optical properties of colloidal noble metal nanostructures with dimensions spanning <1 nm to tens of nanometers. The remainder of this review is organized as follows: Fundamental descriptions of MCD- and MCPL-based magneto-optical responses are provided in Section 2; the size-dependent absorptive (MCD) magneto-optical responses of nanoclusters and plasmonic nanoparticles are described in Section 3; spin-polarized emission from nanoclusters are discussed in Section 4; and a summary and outlook are provided in Section 5. Although several experimental methods for assessing magneto-optical properties exist, this review is restricted to MCD and MCPL and the impacts they have had for understanding the responses of metal nanostructures.

## 2. DESCRIPTIONS OF MAGNETO-OPTICAL RESPONSES

### 2.1. Fundamentals of Magnetic Circular Dichroism

MCD intensity is assigned according to the difference between the absorbance of RCP and LCP light. Often, MCD spectra contain features similar to those found from ultraviolet (UV)-visible absorption spectra (27). However, MCD resolves spin-orbit fine structure states that make up an electronic state manifold. MCD sensitivity to spin is due to polarization-specific selection rules relating to the magnetic quantum number, $M_J$, that describes each distinct fine structure state: $\Delta M_J = 0, \pm 1$. Under field-free, linear absorption conditions, the $M_J$ levels are nearly degenerate. However, in a magnetic field, the $M_J = +1$ $(-1)$ levels align (anti-align) with the applied field vector, resulting in an energy increase (decrease) for the fine structure states. This effect, known as Zeeman splitting, lifts the degeneracy of the spin-orbit fine structure levels (**Figure 2*a***). The magnitude of this effect is directly proportional to the Landé *g*-factor (*g*), which describes the SOC interactions of each $M_J$ state (28) as

$$\Delta E = g\mu_B \vec{H}, \qquad 1.$$

where $\mu_B$ is the Bohr magneton constant, and $\vec{H}$ is the strength of the magnetic field applied parallel to the propagation axis of light. The two Zeeman split $M_J$ components selectively absorb either RCP or LCP light. Hence, a difference spectrum of Abs(lcp) – Abs(rcp) isolates the spin fine structure states. Reversal of the magnetic field direction (i.e., polarity) inverts the Zeeman

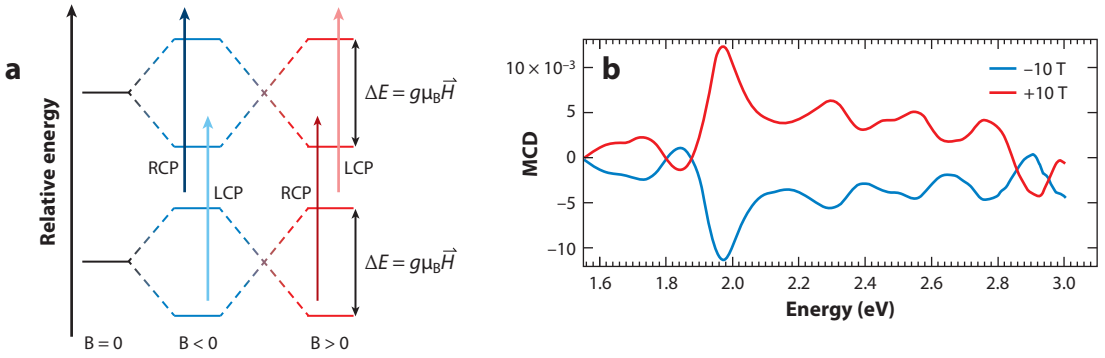


**Figure 2**

(*a*) Depiction of Zeeman splitting under an applied magnetic field, with the energy splitting proportional to the Landé *g*-factor of the transition (*g*), the magnetic field strength ($\vec{H}$), and the Bohr magneton ($\mu_B$). Upon inversion of the applied magnetic field polarity, the Zeeman split states flip in preference for left circularly polarized (LCP) or right circularly polarized (RCP) light. Adapted with permission from Reference 5; copyright 2016 American Chemical Society. (*b*) Magnetic circular dichroism (MCD) response under applied magnetic field of equal magnitude but opposing polarity, showcasing the mirror image spectrum produced.

split states, resulting in polarity-dependent mirror images of the MCD spectra (**Figure 2*b***). This inversion provides experimental validation that peaks detected in the difference spectra result from the magneto-optical properties of the sample (29).

The formalism for MCD intensity, $\Delta A/E$, is given in Equation 2 (30),

$$\frac{\Delta A}{E} = \left(cg\mu_B \vec{H}\right)\left[A_1\left(\frac{\delta f(E)}{\delta(E)}\right) + \left(B_0 + \frac{C_0}{k_B T}\right) f(E)\right], \qquad 2.$$

where $\Delta A$ is the field-dependent difference between the absorption of LCP and RCP light, $E = h\nu$, $c$ is a constant that accounts for path length and sample concentration, $g$ is the Landé $g$-factor, $\mu_B$ is the Bohr magneton, $\vec{H}$ is the applied magnetic field, $f(E)$ is the absorption band shape, and $\delta f(E)/\delta(E)$ is the first derivative. $A_1$, $B_0$, and $C_0$ are the Faraday A, B, and C terms, respectively.

The $A_1$ term arises from the Zeeman splitting of degenerate excited states. Due to the shift in band centers between the two states, the A term is characterized by a distinct derivative lineshape. By convention, a positive A term is typically used for derivative-shaped signals that are positive on the higher-energy end of the feature.

The $B_0$ term arises from the field-induced mixing of zero-field states via magnetic dipole transition moments. Typically, $B_0$ terms also become dominant in MCD spectra in cases in which the sample does not have threefold or higher rotational symmetry, but these terms are present with lower relative contribution in higher symmetry structures as well. They present most often as a Gaussian lineshape in MCD spectra; however, note that structural changes can cause a small zero-field splitting in otherwise degenerate states, causing a derivative lineshape from $B_0$ terms of opposite signs referred to as a pseudo–$A_1$ term.

Lastly, in paramagnetic materials, the $C_0$ term becomes prominent, describing the splitting of degenerate ground states. The population in this case follows a Boltzmann distribution, and so has a $1/kT$ dependence. Due to this dependence, the $C_0$ term is Gaussian shaped and has a clear temperature dependence. This also makes it readily distinguishable from the $B_0$ term despite having similar lineshapes, as the $B_0$ term does not share this dependence.

## 2.2. Magnetic Circular Photoluminescence Spectroscopy

MCPL is the spontaneous emission analog of MCD. Whereas MCD isolates spin-polarized absorptive transitions based on differential extinction of circularly polarized light, MCPL generates differential PL spectra through the collection of circularly polarized emissions following photoexcitation (3, 5, 31, 32). The theoretical description of MCPL closely mirrors those of MCD, described in Section 2.1; both MCD and MCPL originate from the Zeeman splitting of fine structure states induced by an applied magnetic field (31). The Faraday A, B, and C terms all contribute to MCPL spectra. However, in the case of MCPL, information regarding the splitting and near-degenerate zero-field states corresponds primarily to the excited states rather than to the ground states (3). In addition, MCPL makes possible the isolation of transient spin intermediates.

## 2.3. Variable-Temperature, Variable-Field Magnetic Circular Dichroism, and Magnetic Circular Photoluminescence

The information content of both MCD and MCPL measurements can be readily expanded by controlled variation of the sample temperature and applied magnetic field strength. While information regarding the Faraday terms is encoded into any obtained spectra, as seen in Equation 2, a priori knowledge of the magnetic dipole moment is needed to extract this information. Variable-temperature, variable-field (VTV$\vec{H}$) techniques make the relative Faraday term contributions

more accessible, while simultaneously yielding the Landé *g*-factor and zero-field energy splitting of fine structure states (6, 33–41).

Variable-field MCD (V $\vec{H}$-MCD) describes the Landé *g*-factor and Faraday B and C term relative amplitudes ($B_0$ and $C_0$) as

$$\Delta I = \vec{H}B_0 + C_0 \tanh\left(g\mu_B \frac{\vec{H}}{2k_B T}\right), \quad 3.$$

where $\Delta I$ is the magnetic field–dependent MCD intensity of the peak of interest (41, 42).

Variable-temperature (VT-MCD) analysis allows for the quantification of the zero-field energy separation between nearly degenerate fine structure states ($\Delta$). The temperature-dependent MCD response is described as a series

$$\Delta I = \sum_i \frac{C_i}{k_B T}\alpha_i \vec{H} + B_i \alpha_i \vec{H}, \quad 4.$$

$$\alpha_1 = \frac{1}{1 + e^{\frac{-\Delta}{k_B T}}}, \quad 5.$$

where $k_B$ is the Boltzmann constant, $T$ is the temperature in Kelvin, and $B_i$ and $C_i$ represent the *i*th component for the Faraday B and C terms, respectively (41, 42). Combining these techniques has proven to be a useful and robust approach to obtaining electronic structure information for colloidal metal nanoparticles.

## 3. EVOLUTION OF SIZE-DEPENDENT METAL NANOPARTICLE MAGNETIC CIRCULAR DICHROISM RESPONSES

In this section, the MCD response of metal nanostructures spanning the nanocluster (<2 nm) through plasmonic nanoparticle regimes is described. First, the MCD spectra of $Au_{25}(SC_8H_9)_{18}$ (MPC) is detailed. This MPC possesses a 13-atom icosahedral core surrounded by six V-shaped –S–Au–S–Au–S– motifs (14, 15, 43–48). In contrast with plasmonic nanoparticles, both the linear and magneto-optical UV-visible-NIR spectra (**Figure 3*a***) include many discrete peaks. MCD measurements, along with theoretical studies, show that the low-energy intraband transition results from electronic excitation involving superatomic orbitals associated with the MPC core, whereas the cluster's protective ligand shell contributes significantly to the high-energy (>2.5-eV) transitions. Theoretical studies on this system showed that the essentially triply degenerate highest-occupied molecular orbital (HOMO) is delocalized over the gold nanocluster core (46). This orbital has superatomic *P* orbital–like character (see the sidebar titled Superatoms). The lowest-unoccupied molecular orbital (LUMO) and LUMO+1 have superatomic *D* orbital–like characters.

**Figure 3*a*** portrays the 1.6-K MCD spectra of $Au_{25}(SC_8H_9)_{18}$. All MCD peaks shown in **Figure 3*a*** are dominated by C terms or pseudo–A terms with minority B term contributions in some cases. This result is expected given the low sample temperature (1.6 K) and the fact that neutral $Au_{25}(SC_8H_9)_{18}$ is known to be paramagnetic (17); generally, low-temperature signal magnitudes for A:B:C = 1:1:1,500 for paramagnetic samples (36). The power of the VTV$\vec{H}$ method for determining electronic structure is seen in **Figure 3*b***, in which magnetic field–dependent isotherms are given for the LUMO ← HOMO and LUMO ← HOMO − 1 transitions. The two isotherms in **Figure 3*b*** show saturation at high applied magnetic field and are satisfactorily fit using the Brillion-type function shown in Equation 3 (J. Foxley, T.D. Green & K.L. Knappenberger,

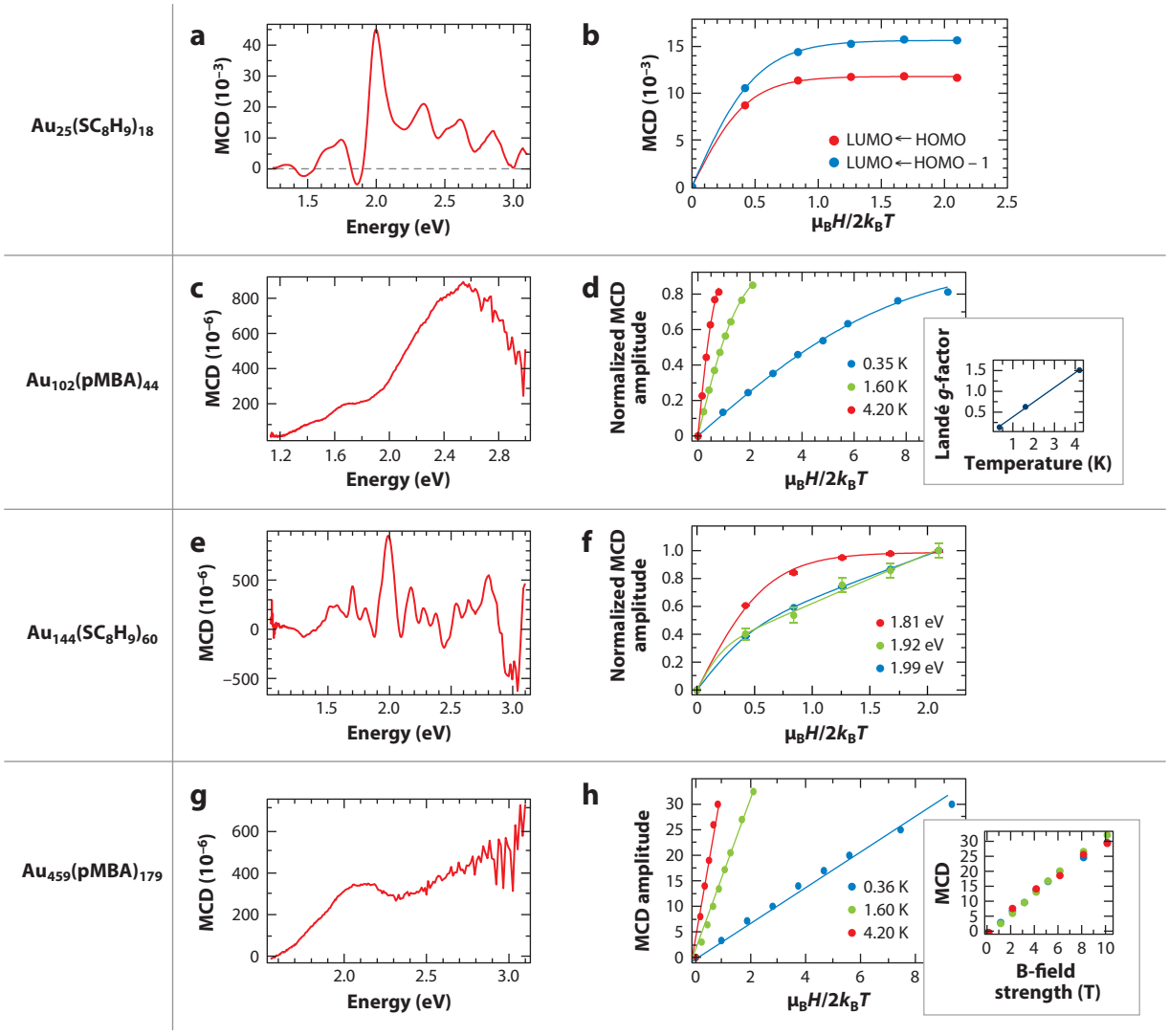


**Figure 3**

Size-dependent gold nanostructure magneto-optical properties. Magnetic circular dichroism (MCD) (*left*) spectra and (*right*) magnetization curves of four distinct clusters: (*a*,*b*) $Au_{25}(SC_8H_9)_{18}$, (*c*,*d*) $Au_{102}(pMBA)_{44}$, (*e*,*f*) $Au_{144}(SC_8H_9)_{60}$, and (*g*,*h*) $Au_{459}(pMBA)_{179}$. Changes in magnetization behavior can be observed, with spectra having increasing complexity and more peaks at larger sizes before one peak dominates at the largest size. Each nanocluster exhibits unique magneto-optical responses. (*a*,*b*) $Au_{25}(SC_8H_9)_{18}$ displays largely superatomic- and molecular-like responses, in which clear discrete transitions are readily observable with primarily C term dependence, displaying clear paramagnetic behavior. (*c*,*d*) $Au_{102}(pMBA)_{44}$ shows a temperature dependence of the observed Landé *g*-factor, suggesting that changes in the lattice dominate the magneto-optical response through rehybridization of Au *d*-band electrons. (*e*,*f*) $Au_{144}(SC_8H_9)_{60}$ exhibits resolvable MCD peaks, in which each shows distinct magneto-optical properties including superatomic and paramagnetic signatures in the magnetization curves. (*g*,*h*) $Au_{459}(pMBA)_{179}$ shows the dominance of a single peak with a primarily linear response, suggesting plasmon-supporting behavior. Panels *c* and *d* are adapted with permission from Reference 10; copyright 2019 American Chemical Society.

## SUPERATOMS

Atomic clusters can mimic the electronic properties of individual atoms, leading to their designation as superatoms. First observed in alkali metal clusters, this behavior extends to clusters of noble metals. Superatom electronic structure can be described by the jellium model, wherein the core is assumed to have a uniform positive charge and spherical symmetry. The valence electrons of the metal behave as free electrons, producing orbitals that are similar to those found in atoms. A principal difference between atomic and superatomic orbitals is noted in the ordering of the orbitals, being characterized as 1*S*, 1*P*, 1*D*, 2*S*, 1*F*, and so on. In cases in which these shells are filled, the resulting cluster shows extraordinary stability and is termed a magic-sized cluster. More information on this subject may be found in Reference 96.



unpublished manuscript). Analysis of the MCD isotherm yields a ground-state Landé *g*-factor of 1.40 ± 0.08, which agrees well with expectations for a seven-electron superatomic *P* orbital with $S = ½$ ($^2P_{3/2}$: $g = 1.33$); *c* is a constant that fits the saturation amplitude of the isotherm. The exact form presented in Equation 3 is restricted to Kramer-type systems with $S = ½$ (38). Less than a 1% B term contribution is detected in the MCD signal, indicating the MCD response was dominated by the paramagnetic superatom. The results obtained from using Equation 3 to describe the MCD data for peaks in the HOMO-LUMO region agree well with previous calculations by Aikens and coworkers (17) for the neutral seven-electron $Au_{25}(SH)_{18}$ system, which concluded that the HOMO was part of the superatom *P* orbital with $S = ½$. The **Figure 3** data are significant because they show that the HOMO-LUMO gap magneto-optical properties of quantum-scale metal nanoclusters can be understood and predicted using superatomic models.

MCD isotherms obtained at excitation energies greater than the HOMO-LUMO transition exhibit more complicated field dependencies. Rather than saturation at high field, the magnetization isotherms for these transitions require larger B term weighting. This behavior is indicative of zero-field splitting in the complex multiplet of fine structure states that comprise the transition ground state and for systems with $S \neq ½$. Future research will need to expand the Brillion-type function (Equation 3) used to fit the isotherms to allow the determination of the ground-state Landé *g*-factors and the magnitude and sign of the transition moments in three dimensions. Theoretical predictions have also shown that $Au_{25}(SH)_{18}$ optical absorption peaks are very sensitive to the electron density in the core, meaning it is important to determine the Au–Au bond distances correctly in a nanoparticle core before predicting its magneto-optical response (49). Therefore, research is needed to understand how synthetic changes such as ligand exchange and metal atom substitution affect the magneto-optical properties of these nanostructures.

In contrast to the multiple discrete MCD peaks observed for $Au_{25}(SC_8H_9)_{18}$, the $Au_{102}(pMBA)_{44}$ cluster exhibits two distinguishable responses spanning the NIR-to-visible regions (10) (**Figure 3*c***). The high-energy region, centered at 2.6 eV, results from metal-based transitions involving the gold *d*-band, and the low-energy regions show a broad peak at 1.6 eV attributed to metal–ligand charge-transfer excitations. In particular, the 2.6-eV feature represents a fundamentally different MCD response than those observed for the smaller, superatomic $Au_{25}(SC_8H_9)_{18}$ and is the smallest known example of a 5*p*-6*d* gold interband MCD response (10).

A unique feature of the $Au_{102}(pMBA)_{44}$ magneto-optical response is the observation of increased MCD intensity as the sample temperature is increased from 350 mK to 4.2 K (**Figure 3*d***). This increase is in contrast to the typical decrease in MCD intensity with increasing sample temperature for paramagnetic C terms and, hence, is not reconciled by changes to the Boltzmann distribution of electronic spin-orbit fine structure states. In fact, the **Figure 3*d*** data (see the inset)

reveal that the Landé *g*-factor for the interband transition increases 15-fold when the sample temperature is increased. This change results from a rehybridization of the *s-p-d* electrons that make up the interband excitation (10, 50, 51). The increased sample temperature allows for lattice expansion, causing the creation of *d*-orbital vacancies, which in turn leads to paramagnetic behavior for the metal nanocluster. This observation suggests that mechanical and synthetic routes to modify nanocluster lattice strain could be effective tools for controlling metal magneto-optical properties.

Moving into increasingly large clusters, MCD analysis has also been done on transitions of $Au_{144}(SC_8H_9)_{60}$ and $Au_{459}(pMBA)_{170}$. These two clusters were selected because the 459-gold atom species is plasmon supporting, and $Au_{144}(SC_8H_9)_{60}$ is among the smallest gold colloids to exhibit metallic electronic behavior (52, 53). Qualitatively, the MCD spectrum obtained for $Au_{144}(SC_8H_9)_{60}$ is far more complex than those seen in either smaller or larger nanoclusters (**Figure 3*e***). In fact, within this spectrum, more than 19 distinct MCD peaks spanning visible excitation energies that exhibit both straightforward and complex assignments of the magneto-optical contributions can be observed. Comparison of the magnetization curves for the 1.92-eV and 1.99-eV peaks exemplifies the complexity and diversity of MCD responses (**Figure 3*f***). Despite being separated by only 70 meV in excitation energy, MCD analysis reveals immediately apparent differences in the spin and orbital angular momenta properties of the electronic transitions that give rise to these peaks. At 1.92 eV, a large Landé *g*-factor of more than 4 was found, in agreement with a dominant G superatom contribution (54, 55). At 1.99 eV, however, the smaller Landé *g*-factor of 2.1 is best accounted for by a mixture of contributions, being in general agreement with superatomic contributions as well as sulfur orbital and interband transitions similar to those seen in $Au_{102}(pMBA)_{44}$. A third distinct type of behavior is observed at 1.81 eV (**Figure 3*f***) that is accurately fit with a single saturating Faraday C term. This behavior is indicative of a paramagnetic center and most likely results from an unpaired electron in a superatomic orbital. Taken together, the 1.99-eV (manifold of states), 1.92-eV (superatomic), and 1.81-eV (paramagnetic) observations show the complexity of magneto-optical effects that can occur for metals in the narrow size range intermediate to both the molecular and metallic regimes. This complexity results from the competing interplay between superatomic, gold interband, and metal–ligand complexes that can all contribute to the magneto-optical response (J. Foxley, T.D. Green & K.L. Knappenberger, unpublished manuscript). All of these contributions also add to the linear extinction measured for these species, but MCD methods are especially powerful for identifying their relative contributions to excitation.

In contrast to $Au_{144}(SC_8H_9)_{60}$, the $Au_{459}(pMBA)_{170}$ MCD spectrum (**Figure 3*g***) exhibits a single peak due to plasmon excitation and a higher-energy feature associated with the interband excitation. Also, in contrast to the magneto-optical responses for all smaller clusters described to this point, the MCD intensity is temperature independent (J. Foxley, T.D. Green & K.L. Knappenberger, unpublished manuscript) (see the inset to **Figure 3*b***). This observation is consistent with seminal studies on plasmon MCD of 25-nm-diameter colloidal gold nanospheres by Mason and coworkers (56) that showed an asymmetric temperature-independent lineshape resulting from Faraday A and B terms. The temperature independence of the plasmon MCD response is attributed to excited-state spin-orbit interactions of the gold 6(*sp*) conduction band. However, when a range of morphologies and dimensions are considered, plasmon-resonant magneto-optical properties are diverse and not always directly attributed to electron spin considerations.

Gold nanorods show a distinctly different response from that shown by the spherical nanoparticles—particularly, although there is still a bisignate response about the transverse surface plasmon resonance (TSPR), the longitudinal surface plasmon resonance (LSPR) appears as a single Gaussian peak. This phenomenon is illustrated in **Figure 4**. To reconcile the distinct TSPR and LSPR MCD responses, the lineshapes were compared against the currently understood molecular

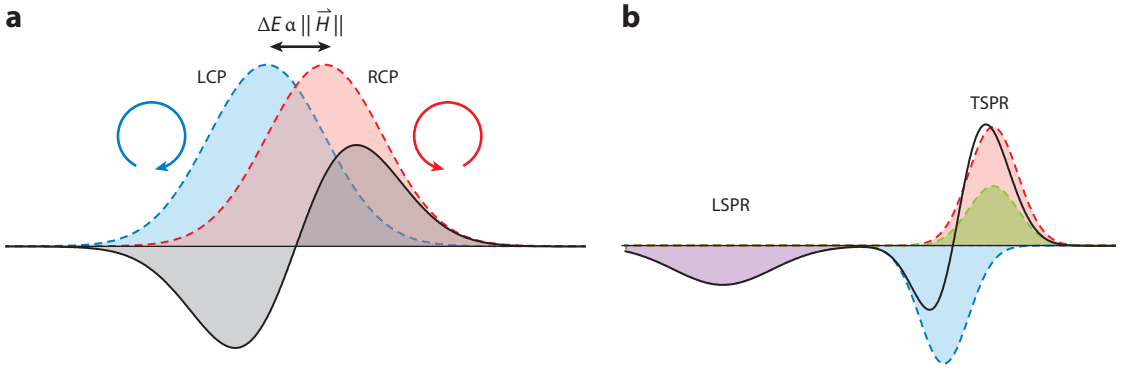


**Figure 4**

(*a*) Rendering of an ideal magnetic circular dichroism (MCD) response of isotropic metal nanospheres. Due to induced circular motion of electrons under plasmon excitation, a magnetic field ($\vec{H}$)-dependent Zeeman splitting effect is observed between left circularly polarized (LCP) (*blue*) and right circularly polarized (RCP) (*red*) light, leading to a bisignate response (*black*) similar to the experimental observations seen in Reference 56. Redrawn with permission from Reference 98; copyright 2013 American Chemical Society. (*b*) Illustration of an idealized MCD response from a metal nanorod, displaying a similar bisignate response to nanospheres at the transverse surface plasmon resonance (TSPR) center, but a single Gaussian response at the longitudinal surface plasmon resonance (LSPR) center. Redrawn with permission from Reference 57; copyright 2017 American Chemical Society.

framework of MCD; the derivative or bisignate shape of the TSPR could be largely correlated to an A term–like response, while the Gaussian response at the LSPR could be explained as being more akin to a B term. This was ascribed to symmetry considerations—rotation about the transverse axis, as would be observed in the TSPR, maintains cylindrical symmetry, while rotation about the longitudinal axis has only twofold rotational symmetry. In cases of low symmetry—having under a threefold axis of rotation—the B term dominates. Therefore, the observed A term–like shape is only apparent in the high-symmetry TSPR, while the LSPR retains a B term. Additionally, increasing the aspect ratio of the nanorods—and therefore increasing the energy difference between LSPR and TSPR—was observed to cause a corresponding decrease in the MCD response of the LSPR, suggesting coupling of the two modes, an assertion supported by the coupling of nonmetallic molecules to metal nanostructures (57, 58). An identical response has been observed in gold nanobipyramid structures, despite having only fivefold symmetry in the TSPR (59), or even nanodisks (60). This observation has opened prospects for the precise tuning of plasmon-mediated magneto-optical properties through synthetic control over the nanostructure aspect ratio.

Structural influences over the magneto-optical responses of noble metal nanoparticles become especially pronounced in multipolar plasmon-supporting systems. In the case of nanoprisms, the SPR is known to have both a dipolar and a quadripolar component (61). Interestingly, the responses of these components were clearly distinct. The dipolar response followed a similar A term–like derivative lineshape, clearly displaying similar behavior to what would typically be expected based on the splitting of degenerate circular plasmon modes. The quadrupolar excitations, however, appear as single Gaussian peaks. In this case, this is potentially due to an inherent difference in the collective excitation of dipolar and quadrupolar localized SPRs. Similar responses have been observed in other nanostructures, such as silver nanodecahedra (29). While the dipolar case allows for the direct formation of a circular oscillation of electrons under an applied magnetic field, a quadrupolar case oscillates along two axes simultaneously. As such, the circular oscillation under an applied magnetic field becomes the sum of two distinct and opposing components, with

energies dependent on the zero-field excitation frequency but not the overall spin of the oscillation. Because of this, the response is small in intensity and has no apparent derivative shape (62).

The size dependence of metal nanostructure MCD properties is clearly varied, evolving with size, composition, and morphology. Plasmonic nanoparticles afford diversity in the polarization and amplitude modulation of incident light. Exploitation of novel plasmon excitation schemes for these types of modulations is an active area of research. The discrete superatomic and molecular-like behavior observed for nanocluster MCD opens possibilities for quantum-state magneto-optical effects.

## 4. SPIN-POLARIZED PHOTOLUMINESCENCE IN SUBNANOMETER GOLD NANOCLUSTERS

### 4.1. Characterization of Nanocluster Excited-State Photoluminescence Transitions

This section describes the use of VTV$\vec{H}$-MCPL to characterize transient excited states and PL mechanisms in gold nanoclusters. The $Au_{25}(SC_8H_9)_{18}^0$ global PL (**Figure 5*a***) spans visible-to-NIR emission. Although the origins of this broad PL have been debated by experimental and theoretical physical chemists, the magneto-optical signatures of $Au_{25}(SC_8H_9)_{18}^0$ show clear evidence for both metal-centered intraband and metal-to-ligand charge-transfer semiring contributions to the global emission. VTV$\vec{H}$-MCPL spectra exhibit three distinct peaks with mean energies of 1.64, 1.78, and 1.94 eV (**Figure 5*a***). The detection of three distinct $Au_{25}(SC_8H_9)_{18}^0$ emission channels is a unique feature of the nanocluster, which differs from expectations for most molecules and colloidal nanoparticles. Rather than the internal carrier relaxation typical for many chromophores, the MCPL spectra suggest photoexcited charge carriers have complex and competing spin-dependent relaxation dynamics. These relaxation pathways were characterized using VTV$\vec{H}$-MCPL spectroscopy in combination with variable-temperature global PL measurements. Analysis of the field-dependent intensity using Equations 3–5 yields Landé *g*-factors of 1.1 ± 0.1, 1.7 ± 0.1, and 1.1 ± 0.1 for the 1.64-eV, 1.78-eV, and 1.94-eV peaks, respectively (**Figure 4*b***). For both the 1.64- and 1.94-eV features, the measured Landé *g*-factor values agree with a $^2D_{5/2}$ term for the excited state. In contrast, the 1.78-eV feature agrees more closely with a $^4P_{3/2}$ or $^4P_{5/2}$ term assignment, suggesting contributions from sulfur *p* orbitals from the semiring unit of the MPC (3, 5). Based on these data, the three spin transitions could be assigned to either metal-centered intraband ($^2$D) or metal-to-ligand interband ($^4$P) radiative relaxation pathways. We note that the $^2$D term reflects the excited superatom *D* orbital of the nanocluster. Based on these results, the lower-energy portion (<1.7 eV) of the spectrum corresponds to intraband relaxation and the high-energy emission (>1.7 eV) results from charge-transfer transitions. The **Figure 5*b*** data qualitatively reflect the similarity of the 1.76- and 1.94-eV signals, which are distinct from that measured at 1.64 eV, explaining the quantitatively different *g* factors and term symbols obtained for the two transition types.

Energy-resolved and temperature-dependent analysis of MCPL signals implicates the interplay between PL and nanocluster nuclear dynamics. The results of this analysis are summarized in **Table 1**. This analysis resolves two distinct vibrational modes with frequencies of ≈150 and 180 $cm^{-1}$, which are assigned to dilation of the metal core and Au–S–C tangential stretching of the semiring, respectively (63, 64). The 150-$cm^{-1}$ dilation mode is most closely associated with the low-energy portion of the emission spectrum, whereas the 180-$cm^{-1}$ stretch is detected for emission at >1.7 eV. These observations support the assignment of the 1.64-eV peak to metal-centered superatomic $^2D \rightarrow {}^2P$ relaxation, while suggesting that the features at 1.78 eV and 1.94 eV proceed through a relaxation channel involving the metal–chalcogenide semirings.

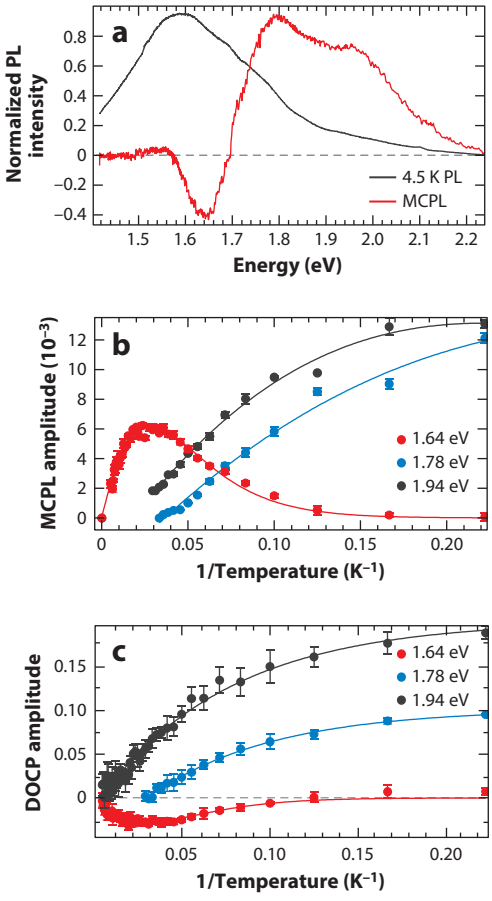


**Figure 5**

The variable-temperature magnetic circular photoluminescence (MCPL) response of $Au_{25}(SC_8H_9)_{18}$. (*a*) Zero-field PL (*black trace*) and MCPL (*red trace*) spectra. (*b*) Temperature dependence of each of the three prominent peaks of the observed MCPL along with fits to Equation 3. (*c*) Temperature dependence of the degree of circular polarization (DOCP) of observed peaks. Increases in both MCPL and DOCP are observed at increased sample temperatures for the 1.64-eV peak, suggesting thermal conversion from a bright state into a dark state, which allows for retention of spin polarization. Adapted with permission from Reference 18; copyright 2021 John Wiley & Sons.

## 4.2. Spin-Polarized Nanocluster Emission

The observed degree of circular polarization (DOCP) is correlated to the type of radiative transition mediating emission. The largest DOCP—approximately 20%—results from states involving interband charge-transfer contributions (18). Temperature-dependent DOCP analysis shows that thermal excitation of the Au–S stretch quenches polarized emission by the charge-transfer states (9, 18). In contrast, intraband relaxation (1.64 eV) shows an increased spin polarization with increasing sample temperature (**Figure 5*c***). This is an unusual temperature dependence and shows prospects for spin-polarized emission at noncryogenic temperatures. The ability to prepare persistent spin-polarized states at operational temperatures is a key requirement for many spin-based quantum information applications. Time-domain data indicate the spin-polarized lifetimes are hundreds of microseconds.

**Table 1 Summary of electronic-vibrational coupling analysis of $Au_{25}(SC_8H_9)_{18}$**

| Peak energy (eV) | Vibrational energy ($cm^{-1}$) | Coupling constant |
|---|---|---|
| 1.64 | 154 +/− 1 | 4.0 +/− 0.1 |
| 1.78 | 178 +/− 2 | 9.0 +/− 0.2 |
| 1.94 | 182 +/− 3 | 4.8 +/− 0.1 |

VTV$\vec{H}$-MCPL spectroscopy was next used to determine the origin of the increased spin polarization that resulted from increasing sample temperature (18). The DOCP signals were fit using a model that invokes an activation barrier ($\Delta$) separating bright and dark fine structure states that form the Faraday C term of a Kramer's doublet according to Equation 6:

$$\mathrm{DOCP} = \frac{\mu_B \vec{H} C}{k_B T} \frac{1}{1 + e^{\frac{-\Delta}{k_B T}}}. \quad 6.$$

Here, C is the C term amplitude, and the remaining terms are as described in Section 2. The basis for using this formalism is that $Au_{25}(SC_8H_9)_{18}$ is paramagnetic, so the magnetization response can be expected to be dominated by the Faraday C term (35). Through a combination of magnetic field and temperature-dependent measurements, the increase in DOCP with increasing sample temperature is determined to result in the thermal population of a bright spin-polarized emissive intraband fine structure state. The 1.64-eV peak consists of a manifold of electronic fine structure states resulting from unique spin and orbital angular momentum coupling. For $Au_{25}(SC_8H_9)_{18}$, an activation energy of 3.3 meV (50 K) for the population of the bright state was determined (67). These data are encouraging because they suggest that fine structure states with appropriate energy gaps may support spin-polarized emission at noncryogenic temperatures. $Au_{25}(SC_8H_9)_{18}$ consists of multiple spin-orbit states with calculated energy gaps exceeding 25 meV ($\sim k_B T$) (65, 66).

The activation barriers to access spin-polarized emission may be even larger in smaller clusters. The NIR intraband PL described in Sections 4.1 and 4.2 has been extended to a series of three gold MPCs with volumes spanning from 50 to 200 $Å^3$ (67). The three MPCs, which included $Au_{20}(SC_8H_9)_{15}$-diglyme, $Au_{25}(SC_8H_9)_{18}$, and $Au_{38}(SC_{12}H_{25})_{24}$, all exhibited temperature-dependent intensities that reflected a few-millielectronvolt energy gap that separated bright emissive and dark nonradiative electronic states. All clusters showed increased PL intensities and DOCP upon raising the sample temperature from 4.5 K to a cluster-specific value (67). Importantly, the results show evidence of a common and size-scalable metal-centered intraband PL mechanism that is general for ultrasmall metal nanoclusters. The resultant degree of spin polarization is a result of the extent of mixing between the bright and dark states. Moreover, the energy gap separating the bright and dark states is directly determined by the domain size of the nanoclusters, resulting in spin-polarized emission up to 160 K (67). These results indicate that structurally precise MPCs may provide a platform for designing nanoscale metals with spin-selective and spin-polarized optical properties. The findings also provide key new fundamental insights for understanding emission from nanoscale metals. Prior to these reports, the general consensus was that gold domains in this size range do not present size-scalable properties (68, 69). The energy gap separating optically bright and dark SOC fine structure states is the first general and size-dependent effect for quantum-confined gold nanoclusters (67).

### 4.3. The Influence of Metal–Atom Substitution on Nanocluster Magnetic Circular Photoluminescence

Using VTV$\vec{H}$-MCPL, the influence of metal–atom substitution on nanocluster emission yields and degrees of spin polarization was determined (9). In one case study, the emission properties of

$Au_{24}Pd(SC_8H_9)_{18}$ were compared with those of $Au_{25}(SC_8H_9)_{18}$. Pd-atom substitution occurs at the 13-metal atom kernel of the nanocluster, and as a result the icosahedral symmetry is retained for both species (70–72). However, the difference in electron count results in a six- rather than a seven-electron superatom for the Pd-substituted nanocluster. Qualitatively, both nanoclusters exhibit similar MCPL spectra with three distinct components resolved. This qualitative similarity is evidence that structural changes due to metal–atom substitution at the core are insignificant. However, quantitative differences are observed in the low-energy MCPL emission. The 1.64-eV peak observed for $Au_{25}(SC_8H_9)_{18}$ is blue-shifted by ≈40 meV upon Pd substitution. This energy shift is attributed to differences in the electronic filling of the nanocluster superatomic *P* levels. Variable-field analysis of each MCPL component revealed an increase in spin-orbit coupling (Landé *g*-factor) magnitudes for radiative transitions of the Pd-substituted cluster with respect to $Au_{25}(SC_8H_9)_{18}$ (9). Variable-temperature PL spectroscopy results indicated that Pd substitution for Au in $Au_{25}(SC_8H_9)_{18}$ resulted in increased angular momenta for metal–metal intraband transitions; the Landé *g*-factor for these transitions increased by ≈55% upon substitution, compared with an approximate 19% increase for semiring-based transitions. The increased angular momentum translated to a 30% increase in electron–phonon coupling constants for intraband transitions but to only a 3% increase for ligand-based transitions. As a result, Pd substitution leads to less efficient metal–metal (intraband) radiative emission for $Au_{24}Pd(SC_8H_9)_{18}$ than for $Au_{25}(SC_8H_9)_{18}$. Importantly, the results show the sensitivity of nanocluster magneto-optical properties to structure.

A general and important outcome from the VTV$\vec{H}$-MCPL studies on $Au_{24}Pd(SC_8H_9)_{18}$ and $Au_{25}(SC_8H_9)_{18}$ is the direct relationship between nanocluster Landé *g*-factors and electron-vibrational coupling constants. The strong correlation between electronic and spin angular momentum and electron-vibrational coupling is summarized in **Figure 6*b***. Further research is needed to understand the interplay between electronic and nuclear dynamics in nanoscale metal. From a molecular perspective, vibrational (i.e., linear) and spin (i.e., angular) momenta may not be expected to couple. However, theoretical treatments of electron transfer at interfaces predict a spin-dependent so-called friction that determines the electron-vibrational coupling (73). The experimental results shown in **Figure 6** make clear the interplay between nanocluster spin and

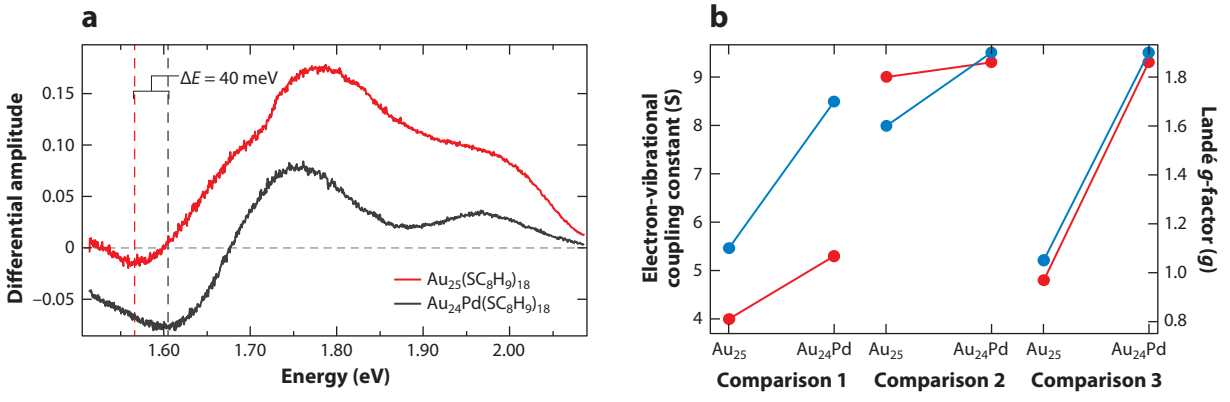


**Figure 6**

Comparison of magnetic circular photoluminescence response between $Au_{25}(SC_8H_9)_{18}$ and $Au_{24}Pd(SC_8H_9)_{18}$ to determine the influence of metal–atom substitution on the magneto-optical properties of the nanocluster. (*a*) Magnetic circular dichroism spectra of both clusters, showing a ≈40-meV blue-shift of the peak at approximately 1.56 eV. (*b*) Comparison of the calculated electron-vibrational coupling constants and Landé *g*-factors. Increases in both are seen upon metal–atom substitution. Adapted with permission from Reference 9; copyright 2021 American Chemical Society.

vibrational dynamics. Generalizable models that account for the origin of these effects will be needed to tailor nanoscale metals with the desired spin properties.

## 5. SUMMARY AND OUTLOOK

The magneto-optical properties of colloidal metal nanostructures have been reviewed. Using MPCs as model systems, the transition from discrete orbital-based absorption to plasmon-mediated extinction was shown to occur for colloidal diameters larger than ≈2 nm. In the plasmonic regime, the MCD frequencies and lineshapes can be modulated by tuning nanoparticle dimensions and shape. These findings indicate that colloidal synthesis can be used to tailor polarization, frequency, and amplitude modulation of light through magneto-optical effects. Hence, the magneto-optical properties of metal nanostructures could have impacts in integrated circuits, molecular sensing, and applied spectroscopy. As is the case with many colloidal nanoparticles, sample inhomogeneity provides some limit to the accuracy of structure-property correlations (74–81). As an absorption technique, MCD is typically restricted to ensemble measurements. Recently, Orrit and coworkers (82) have demonstrated photothermal-based MCD using magnetic nanoparticles. In the future, this method may be extended to metal nanoparticles, enabling single-structure studies of nanoparticle magneto-optical absorption properties.

The MCD studies described in Section 3 identify subnanometer gold nanoclusters as potential candidates for spin-polarized emission. Recent advances in metal nanocluster synthesis have produced colloids with emission yields exceeding 71% (83) and with degrees of spin polarization that are on par with leading quantum materials (18, 84, 85). However, much fundamental research is needed to understand spin-state dynamics in quantum-confined nanoclusters. For example, the relative contributions of metal-centered, superatomic, and semiring states to spin-polarized emission must be understood. Predictive descriptions of how atomic-level structural changes affect these weights are also needed. An important, fundamental question that must be addressed involves the interplay between spin and vibrational modes. MCPL data clearly implicate mode-selective electron-vibrational coupling as a nonradiative decay channel that competes with spin-polarized emission. However, mechanistic understanding regarding how vibrational modes mediate electronic relaxation to specific spin-polarized intermediates is still needed. MCPL studies of MPCs will be especially valuable for developing these mechanistic insights. Additionally, MPCs may provide a model system for understanding how to control these effects synthetically. For example, ligand substitution in gold nanoclusters can result in compression or expansion of the metal core, and in specific cases alters Au–Au and Au–S bond lengths by as much as 50% (63, 64). Because low-frequency vibrations such as core dilation, Au–S stretching, and Au–S–C bending all assist in $Au_{25}(SC_8H_9)_{18}$ carrier relaxation (86–88), these structural changes are expected to affect the distribution of spin-polarized states in these clusters. The results reviewed in Section 4 suggest $Au_{25}(SC_8H_9)_{18}$ is an ideal prototype for understanding the role of intrinsic structural effects in determining nanocluster magneto-optical properties (3, 5, 16, 18). The use of intrinsic forces for controlling electron dynamics should be generalizable over a range of cluster sizes, compositions, and emission wavelengths. Phosphine-protected gold nanoclusters with fewer than ≈11 metal atoms are very flexible and can be forced into strained geometries, including chiral ones, through ligand substitution (89). Clearly, MPCs provide excellent opportunities to deepen our understanding of spin dynamics and magneto-optical properties in metal nanostructures.

Electronic spin plays an important role in many chemical and energy conversion processes of widespread importance. For example, spin polarization has been used to suppress charge carrier recombination in organic photovoltaics, improving device performance (90). The persistence of radical spin intermediates is believed to be responsible for magnetoreception in migratory animals (91). Spin injection into molecules has expanded the field of spintronics to include

molecular electronics. Chiral-induced spin selectivity (CISS) has recently emerged as a subset of spin chemistry (92). CISS refers to the strong influence of enantiomeric structure on electronic spin polarization (93). This effect suggests that material/molecular handedness can be used to control chemical properties such as molecular shape and reactivity, as well as the outcomes of surface-catalyzed reactions such as water oxidation. Therefore, improved understanding of spin dynamics gained using metal nanostructures may be general and leveraged for impacts in many areas. MCD has similarly been used to inform our understanding of spin-dependent biological processes such as photosynthesis, wherein the oxygen evolution complex has been shown to concentrate high electron spin to interact with triplet oxygen molecules, suggesting the potential for further mechanistic characterization of similar oxygen-reacting systems via transient magneto-optical methods (94, 95). Continued advances in magneto-optical measurement techniques will undoubtedly provide further opportunities to understand spin dynamics and energy flow for a variety of other chemical, biological, and materials systems.

### SUMMARY POINTS

1. Magnetic circular dichroism (MCD) and magnetic circular photoluminescence, based on the Zeeman effect, are two powerful methods for characterizing the magneto-optical properties of metal nanostructures.
2. Plasmonic nanoparticles exhibit mode-specific MCD signals that can be frequency, polarization, and amplitude modulated by nanostructure shape, size, and composition.
3. Magneto-optical spectra of noble metal nanoclusters arise from discrete electronic transitions between superatomic, metallic interband, and/or molecular-like orbitals.
4. Spin-orbit coupling is required to assign the magneto-optical spectra of metal nanoclusters.
5. Gold nanoclusters exhibit quantum-state-specific spin-polarized emission, which is affected by metal atom and ligand substitution.

## DISCLOSURE STATEMENT

The authors are not aware of any affiliations, memberships, funding, or financial holdings that might be perceived as affecting the objectivity of this review.

## ACKNOWLEDGMENTS

The authors gratefully acknowledge the National Science Foundation (grants CHE-1807999, CHE190476, and CHE-2204190) and the Air Force Office of Scientific Research (grants FA9550-18-1-0347 and FA9550-22-1-0402) for support of this work.

## LITERATURE CITED

1. Yao H. 2012. On the electronic structures of $Au_{25}(SR)_{18}$ clusters studied by magnetic circular dichroism spectroscopy. *J. Phys. Chem. Lett.* 3(12):1701–6
2. Jaw HRC, Savas MM, Rogers RD, Mason WR. 1989. Crystal structures and solution electronic absorption and MCD spectra for perchlorate and halide salts of binuclear gold(I) complexes containing bridging Me2PCH2PMe2(dmpm) or Me2PCH2CH2PMe2(dmpe) ligands. *Inorg. Chem.* 28(6):1028–37

3. Herbert PJ, Mitra U, Knappenberger KL. 2017. Variable-temperature variable-field magnetic circular photoluminescence (VTVH-MCPL) spectroscopy for electronic-structure determination in nanoscale chemical systems. *Opt. Lett.* 42(23):4833–36
4. Green TD, Yi C, Zeng C, Jin R, McGill S, Knappenberger KL Jr. 2014. Temperature-dependent photoluminescence of structurally-precise quantum-confined $Au_{25}(SC_8H_9)_{18}$ and $Au_{38}(SC_{12}H_{25})_{24}$ metal nanoparticles. *J. Phys. Chem. A* 118(45):10611–21
5. Green TD, Herbert PJ, Yi C, Zeng C, McGill S, et al. 2016. Characterization of emissive states for structurally precise $Au_{25}(SC_8H_9)_{18}{}^0$ monolayer-protected gold nanoclusters using magnetophotoluminescence spectroscopy. *J. Phys. Chem. C* 120(31):17784–90
6. Jaw HRC, Mason WR. 1991. Magnetic circular dichroism spectra for the octakis(triphenylphosphino)-nonagold(3+) ion. *Inorg. Chem.* 30(2):275–78
7. Jiang DE, Kühn M, Tang Q, Weigend F. 2014. Superatomic orbitals under spin-orbit coupling. *J. Phys. Chem. Lett.* 5(19):3286–89
8. Mishra S, Vallet V, Domcke W. 2006. Importance of spin-orbit coupling for the assignment of the photodetachment spectra of $AuX_2{}^-$ (X = Cl, Br, and I). *ChemPhysChem* 7(3):723–27
9. Herbert PJ, Tofanelli MA, Ackerson CJ, Knappenberger KL Jr. 2021. The influence of Pd-atom substitution on $Au_{25}(SC_8H_9)_{18}$ cluster photoluminescence. *J. Phys. Chem. C* 125(13):7267–75
10. Herbert PJ, Window P, Ackerson CJ, Knappenberger KL Jr. 2019. Low-temperature magnetism in nanoscale gold revealed through variable-temperature magnetic circular dichroism spectroscopy. *J. Phys. Chem. Lett.* 10(2):189–93
11. Tsesses S, Cohen K, Ostrovsky E, Gjonaj B, Bartal G. 2019. Spin-orbit interaction of light in plasmonic lattices. *Nano Lett.* 19(6):4010–16
12. Zhu M, Aikens CM, Hollander FJ, Schatz GC, Jin R. 2008. Correlating the crystal structure of a thiol-protected $Au_{25}$ cluster and optical properties. *J. Am. Chem. Soc.* 130(18):5883–85
13. Jadzinsky PD, Calero G, Ackerson CJ, Bushnell DA, Kornberg RD. 2007. Structure of a thiol monolayer-protected gold nanoparticle at 1.1 Å resolution. *Science* 318(5849):430–33
14. Walter M, Akola J, Lopez-Acevedo O, Jadzinsky PD, Calero G, et al. 2008. A unified view of ligand-protected gold clusters as superatom complexes. *PNAS* 105(27):9157–62
15. Heaven MW, Dass A, White PS, Holt KM, Murray RW. 2008. Crystal structure of the gold nanoparticle $[N(C_8H_{17})_4][Au_{25}(SCH_2CH_2Ph)_{18}]$. *J. Am. Chem. Soc.* 130(12):3754–55
16. Williams LJ, Herbert PJ, Tofanelli MA, Ackerson CJ, Knappenberger KL Jr. 2019. Superatom spin-state dynamics of structurally precise metal monolayer-protected clusters (MPCs). *J. Chem. Phys.* 150(10):101102
17. Zhu M, Aikens CM, Hendrich MP, Gupta R, Qian H, et al. 2009. Reversible switching of magnetism in thiolate-protected $Au_{25}$ superatoms. *J. Am. Chem. Soc.* 131(7):2490–92
18. Herbert PJ, Knappenberger KL. 2021. Spin-polarized photoluminescence in $Au_{25}(SC_8H_9)_{18}$ monolayer-protected clusters. *Small* 17(27):2004431
19. Agrachev M, Antonello S, Dainese T, Ruzzi M, Zoleo A, et al. 2017. Magnetic ordering in gold nanoclusters. *ACS Omega* 2(6):2607–17
20. Mustalahti S, Myllyperkiö P, Malola S, Lahtinen T, Salorinne K, et al. 2015. Molecule-like photodynamics of $Au_{102}(p\text{MBA})_{44}$ nanocluster. *ACS Nano* 9(3):2328–35
21. Green TD, Knappenberger KL Jr. 2012. Relaxation dynamics of $Au_{25}L_{18}$ nanoclusters studied by femtosecond time-resolved near infrared transient absorption spectroscopy. *Nanoscale* 4(14):4111–18
22. Jin R, Zeng C, Zhou M, Chen Y. 2016. Atomically precise colloidal metal nanoclusters and nanoparticles: fundamentals and opportunities. *Chem. Rev.* 116(18):10346–413
23. Compel WS, Wong OA, Chen X, Yi C, Geiss R, et al. 2015. Dynamic diglyme-mediated self-assembly of gold nanoclusters. *ACS Nano* 9(12):11690–98
24. Briat B, Djerassi C. 1968. Applications of magnetic circular dichroism and optical rotatory dispersion measurements. *Nature* 217(5132):918–22
25. Foss JG, McCarville ME. 1965. Magnetic circular dichroism and magnetic optical rotatory dispersion. *J. Am. Chem. Soc.* 87(2):228–30
26. Blumling DE, McGill S, Knappenberger KL Jr. 2013. The influence of applied magnetic fields on the optical properties of zero- and one-dimensional CdSe nanocrystals. *Nanoscale* 5(19):9049–56

27. Larrabee JA, Leung CH, Moore RL, Thamrong-nawasawat T, Wessler BSH. 2004. Magnetic circular dichroism and cobalt(II) binding equilibrium studies of *Escherichia coli* methionyl aminopeptidase. *J. Am. Chem. Soc.* 126(39):12316–24
28. King GW. 1965. *Spectroscopy and Molecular Structure*. New York: Holt, Rinehart & Winston
29. Sato H, Yao H. 2019. Application of magnetic circular dichroism (MCD) to morphological quality evaluation of silver nanodecahedra. *Chem. Phys. Lett.* 732:136637
30. Mason WR. 2007. *Magnetic Circular Dichroism Spectroscopy*. Hoboken, NJ: John Wiley & Sons
31. Piepho S, Schatz P. 1983. *Group Theory in Spectroscopy with Applications to Magnetic Circular Dichroism*. Hoboken, NJ: John Wiley & Sons
32. Sutherland JC, Low H. 1976. Fluorescence-detected magnetic circular dichroism of fluorescent and nonfluorescent molecules. *PNAS* 73(2):276–80
33. Archer PI, Santangelo SA, Gamelin DR. 2007. Direct observation of sp–d exchange interactions in colloidal $Mn^{2+}$- and $Co^{2+}$-doped CdSe quantum dots. *Nano Lett.* 7(4):1037–43
34. Neese F, Zaleski JM, Loeb Zaleski K, Solomon EI. 2000. Electronic structure of activated bleomycin: oxygen intermediates in heme versus non-heme iron. *J. Am. Chem. Soc.* 122(47):11703–24
35. Neese F, Solomon EI. 1999. MCD *C*-term signs, saturation behavior, and determination of band polarizations in randomly oriented systems with spin $S \geq 1/2$. Applications to $S = 1/2$ and $S = 5/2$. *Inorg. Chem.* 38(8):1847–65
36. Gewirth AA, Solomon EI. 1988. Electronic structure of plastocyanin: excited state spectral features. *J. Am. Chem. Soc.* 110(12):3811–19
37. Kuno M, Nirmal M, Bawendi MG, Efros A, Rosen M. 1998. Magnetic circular dichroism study of CdSe quantum dots. *J. Chem. Phys.* 108(10):4242–47
38. Solomon EI, Pavel EG, Loeb KE, Campochiaro C. 1995. Magnetic circular dichroism spectroscopy as a probe of the geometric and electronic structure of non-heme ferrous enzymes. *Coord. Chem. Rev.* 144:369–460
39. Ando K, Yamada Y, Shakin VA. 1993. Magneto-optical study of quantum confinement in Cd(S,Se) quantum dots. *Phys. Rev. B* 47(20):13462–65
40. Stephens PJ, McKenna CE, Smith BE, Nguyen HT, McKenna MC, et al. 1979. Circular dichroism and magnetic circular dichroism of nitrogenase proteins. *PNAS* 76(6):2585–89
41. Stephens PJ. 1976. Magnetic circular dichroism. *Adv. Chem. Phys.* 35:197–266
42. Schatz PN, Mowery RL, Krausz ER. 1978. M.C.D./M.C.P.L. saturation theory with application to molecules in Dαk and its subgroups. *Mol. Phys.* 35(6):1537–57
43. Aikens CM. 2010. Geometric and electronic structure of $Au_{25}(SPhX)_{18}^-$ (X = H, F, Cl, Br, $CH_3$, and $OCH_3$). *J. Phys. Chem. Lett.* 1(17):2594–99
44. Jin R. 2010. Quantum sized, thiolate-protected gold nanoclusters. *Nanoscale* 2(3):343–62
45. Price RC, Whetten RL. 2005. All-aromatic, nanometer-scale, gold-cluster thiolate complexes. *J. Am. Chem. Soc.* 127(40):13750–51
46. Aikens CM. 2011. Electronic structure of ligand-passivated gold and silver nanoclusters. *J. Phys. Chem. Lett.* 2(2):99–104
47. Wyrwas RB, Alvarez MM, Khoury JT, Price RC, Schaaff TG, Whetten RL. 2007. The colours of nanometric gold. *Eur. Phys. J. D* 43(1–3):91–95
48. Zheng J, Zhou C, Yu M, Liu J. 2012. Different sized luminescent gold nanoparticles. *Nanoscale* 4(14):4073–83
49. Aikens CM. 2012. Modelling small gold and silver nanoparticles with electronic structure methods. *Mol. Simul.* 38(8–9):607–14
50. Crespo P, Litrán R, Rojas TC, Multigner M, de la Fuente JM, et al. 2004. Permanent magnetism, magnetic anisotropy, and hysteresis of thiol-capped gold nanoparticles. *Phys. Rev. Lett.* 93(8):87204
51. Negishi Y, Tsunoyama H, Suzuki M, Kawamura N, Matsushita MM, et al. 2006. X-ray magnetic circular dichroism of size-selected, thiolated gold clusters. *J. Am. Chem. Soc.* 128(37):12034–35
52. Yi C, Zheng H, Tvedte LM, Ackerson CJ, Knappenberger KL Jr. 2015. Nanometals: identifying the onset of metallic relaxation dynamics in monolayer-protected gold clusters using femtosecond spectroscopy. *J. Phys. Chem. C* 119(11):6307–13

53. Yi C, Tofanelli MA, Ackerson CJ, Knappenberger KL Jr. 2013. Optical properties and electronic energy relaxation of metallic $Au_{144}(SR)_{60}$ nanoclusters. *J. Am. Chem. Soc.* 135(48):18222–28
54. Malola S, Lehtovaara L, Häkkinen H. 2014. TDDFT analysis of optical properties of thiol monolayer-protected gold and intermetallic silver-gold $Au_{144}(SR)_{60}$ and $Au_{84}Ag_{60}(SR)_{60}$ clusters. *J. Phys. Chem. C* 118(34):20002–8
55. Malola S, Kaappa S, Häkkinen H. 2019. Role of nanocrystal symmetry in the crossover region from molecular to metallic gold nanoparticles. *J. Phys. Chem. C* 123(33):20655–63
56. Zaitoun MA, Mason WR, Lin CT. 2001. Magnetic circular dichroism spectra for colloidal gold nanoparticles in xerogels at 5.5 K. *J. Phys. Chem. B* 105(29):6780–84
57. Han B, Gao X, Shi L, Zheng Y, Hou K, et al. 2017. Geometry-modulated magnetoplasmonic optical activity of Au nanorod-based nanostructures. *Nano Lett.* 17(10):6083–89
58. Melnikau D, Govyadinov AA, Sánchez-Iglesias A, Grzelczak M, Liz-Marzán LM, Rakovich YP. 2017. Strong magneto-optical response of nonmagnetic organic materials coupled to plasmonic nanostructures. *Nano Lett.* 17(3):1808–13
59. Han B, Sun C, Zhou Y, Gao X. 2022. Geometry-modulated magnetoplasmonic circular dichroism of gold nanobipyramids. *J. Phys. Chem. C* 126(7):3600–3605
60. Sepúlveda B, González-Diaz JB, Garcia-Martin A, Lechuga LM, Armelles G. 2010. Plasmon-induced magneto-optical activity in nanosized gold disks. *Phys. Rev. Lett.* 104(14):147401
61. Shuford KL, Ratner MA, Schatz GC. 2005. Multipolar excitation in triangular nanoprisms. *J. Chem. Phys.* 123(11):114713
62. Yao H, Shiratsu T. 2017. Multipolar surface magnetoplasmon resonances in triangular silver nanoprisms studied by MCD spectroscopy. *J. Phys. Chem. C* 121(1):761–68
63. Sels A, Salassa G, Pollitt S, Guglieri C, Rupprechter G, et al. 2017. Structural investigation of the ligand exchange reaction with rigid dithiol on doped (Pt, Pd) $Au_{25}$ clusters. *J. Phys. Chem. C* 121(20):10919–26
64. Varnholt B, Oulevey P, Luber S, Kumara C, Dass A, Bürgi T. 2014. Structural information on the Au-S interface of thiolate-protected gold clusters: a Raman spectroscopy study. *J. Phys. Chem. C* 118(18):9604–11
65. Aikens CM. 2018. Electronic and geometric structure, optical properties, and excited state behavior in atomically precise thiolate-stabilized noble metal nanoclusters. *Acc. Chem. Res.* 51(12):3065–73
66. Weerawardene KLDM, Pandeya P, Zhou M, Chen Y, Jin R, Aikens CM. 2019. Luminescence and electron dynamics in atomically precise nanoclusters with eight superatomic electrons. *J. Am. Chem. Soc.* 141(47):18715–26
67. Herbert PJ, Ackerson CJ, Knappenberger KL Jr. 2021. Size-scalable near-infrared photoluminescence in gold monolayer protected clusters. *J. Phys. Chem. Lett.* 12(31):7531–36
68. Bonačić-Koutecký V, Antoine R. 2019. Enhanced two-photon absorption of ligated silver and gold nanoclusters: theoretical and experimental assessments. *Nanoscale* 11(26):12436–48
69. Knoppe S, Verbiest T. 2017. Resonance enhancement of nonlinear optical scattering in monolayer-protected gold clusters. *J. Am. Chem. Soc.* 139(42):14853–56
70. Kacprzak KA, Lehtovaara L, Akola J, Lopez-Acevedo O, Häkkinen H. 2009. A density functional investigation of thiolate-protected bimetal $PdAu_{24}(SR)_{18}^{z}$ clusters: doping the superatom complex. *Phys. Chem. Chem. Phys.* 11(33):7123–29
71. Yan J, Su H, Yang H, Malola S, Lin S, et al. 2015. Total structure and electronic structure analysis of doped thiolated silver $[Mag_{24}(SR)_{18}]^{2-}$ (M = Pd, Pt) clusters. *J. Am. Chem. Soc.* 137(37):11880–83
72. Alkan F, Pandeya P, Aikens CM. 2019. Understanding the effect of doping on energetics and electronic structure for $Au_{25}$, $Ag_{25}$, and $Au_{38}$ clusters. *J. Phys. Chem. C* 123(14):9516–27
73. Teh H-H, Dou W, Subotnik JE. 2021. Antisymmetric Berry frictional force at equilibrium in the presence of spin-orbit coupling. *Phys. Rev. B* 104(20):L201409
74. Willets KA, Van Duyne RP. 2007. Localized surface plasmon resonance spectroscopy and sensing. *Annu. Rev. Phys. Chem.* 58:267–97
75. Chandra M, Dowgiallo A-M, Knappenberger KL Jr. 2012. Magnetic dipolar interactions in solid gold nanosphere dimers. *J. Am. Chem. Soc.* 134(10):4477–80
76. Biswas S, Liu X, Jarrett JW, Brown D, Pustovit V, et al. 2015. Nonlinear chiro-optical amplification by plasmonic nanolens arrays formed via directed assembly of gold nanoparticles. *Nano Lett.* 15(3):1836–42

77. Liu X, Biswas S, Jarrett JW, Poutrina E, Urbas A, et al. 2015. Deterministic construction of plasmonic heterostructures in well-organized arrays for nanophotonic materials. *Adv. Mater.* 27(45):7314–19
78. Li Z, Kang L, Lord RW, Park K, Gillman A, et al. 2022. Plasmon-mediated chiroptical second harmonic generation from seemingly achiral gold nanorods. *ACS Nanosci. Au* 2(1):32–39
79. Ma W, Xu L, de Moura AF, Wu X, Kuang H, et al. 2017. Chiral inorganic nanostructures. *Chem. Rev.* 117(12):8041–93
80. Hazra B, Dey J, Chandra M. 2018. Structure-specific chiroptical responses of hollow gold nanoprisms. *Phys. Chem. Chem. Phys.* 20(43):27675–83
81. Smith KW, Link S, Chang W-S. 2017. Optical characterization of chiral plasmonic nanostructures. *J. Photochem. Photobiol. C* 32:40–57
82. Spaeth P, Adhikari S, Lahabi K, Baaske MD, Wang Y, Orrit M. 2022. Imaging the magnetization of single magnetite nanoparticle clusters via photothermal circular dichroism. *Nano Lett.* 22(9):3645–50
83. Yongbo S, Yingwei L, Meng Z, Xuan L, Hao L, et al. 2022. Ultrabright Au@$Cu_{14}$ nanoclusters: 71.3% phosphorescence quantum yield in non-degassed solution at room temperature. *Sci. Adv.* 7(2):eabd2091
84. Siebers B, Biadala L, Yakovlev DR, Rodina AV, Aubert T, et al. 2015. Exciton spin dynamics and photoluminescence polarization of CdSe/CdS dot-in-rod nanocrystals in high magnetic fields. *Phys. Rev. B* 91(15):155304
85. Barman PK, Sarma PV, Shaijumon MM, Kini RN. 2019. High degree of circular polarization in $WS_2$ spiral nanostructures induced by broken symmetry. *Sci. Rep.* 9:2784
86. Yousefalizadeh G, Stamplecoskie KG. 2018. A single model for the excited-state dynamics of $Au_{18}(SR)_{14}$ and $Au_{25}(SR)_{18}$ clusters. *J. Phys. Chem. A* 122(35):7014–22
87. Stoll T, Sgrò E, Jarrett JW, Réhault J, Oriana A, et al. 2016. Superatom state-resolved dynamics of the $Au_{25}(SC_8H_9)_{18}^-$ cluster from two-dimensional electronic spectroscopy. *J. Am. Chem. Soc.* 138(6):1788–91
88. Yau SH, Varnavski O, Goodson T. 2013. An ultrafast look at Au nanoclusters. *Acc. Chem. Res.* 46(7):1506–16
89. Zhu Y, Guo J, Qiu X, Zhao S, Tang Z. 2021. Optical activity of chiral metal nanoclusters. *Acc. Mater. Res.* 2(1):21–35
90. Rao A, Chow PCY, Gélinas S, Schlenker CW, Li C-Z, et al. 2013. The role of spin in the kinetic control of recombination in organic photovoltaics. *Nature* 500(7463):435–39
91. Wiltschko R, Wiltschko W. 2019. Magnetoreception in birds. *J. R. Soc. Interface* 16(158):20190295
92. Rosenberg RA, Abu Haija M, Ryan PJ. 2008. Chiral-selective chemistry induced by spin-polarized secondary electrons from a magnetic substrate. *Phys. Rev. Lett.* 101(17):178301
93. Naaman R, Paltiel Y, Waldeck DH. 2020. Chiral induced spin selectivity gives a new twist on spin-control in chemistry. *Acc. Chem. Res.* 53(11):2659–67
94. Koperski M, Molas MR, Arora A, Nogajewski K, Bartos M, et al. 2018. Orbital, spin, and valley contributions to Zeeman splitting of excitonic resonances in $MoSe_2$, $WSe_2$, and $WS_2$ monolayers. *2D Mater.* 6:015001
95. Yang K, Tang C, Kuang T, Tang P, Shen Z, et al. 1997. Magnetic circular dichroism of Photosystem II reaction center complex. *Chin. Sci. Bull.* 42(9):784–87
96. Jena P, Sun Q, eds. 2021. *Superatoms: Principles, Synthesis and Applications*. Hoboken, NJ: John Wiley & Sons
97. Zhao T, Herbert PJ, Zheng H, Knappenberger KL Jr. 2018. State-resolved metal nanoparticle dynamics viewed through the combined lenses of ultrafast and magneto-optical spectroscopies. *Acc. Chem. Res.* 51(6):1433–42
98. Pineider F, Campo G, Bonanni V, de Julián Fernández C, Mattei G, et al. 2013. Circular magnetoplasmonic modes in gold nanoparticles. *Nano Lett.* 13(10):4785–89

Annual Review of
Physical Chemistry
Volume 74, 2023

# Contents

**Errata**

An online log of corrections to *Annual Review of Physical Chemistry* articles may be found at http://www.annualreviews.org/errata/physchem